NANO LETTERS

Letter

pubs.acs.org/NanoLett

Near-Field Infrared Vibrational Dynamics and Tip-Enhanced Decoherence

Xiaoji G. Xu and Markus B. Raschke*

Department of Physics, Department of Chemistry, and JILA, University of Colorado, Boulder, Colorado 80309, United States

Supporting Information

ABSTRACT: Ultrafast infrared spectroscopy can reveal the dynamics of vibrational excitations in matter. In its conventional far-field implementation, however, it provides only limited insight into nanoscale sample volumes due to insufficient spatial resolution and sensitivity. Here, we combine scattering-scanning near-field optical microscopy (*s*-SNOM) with femtosecond infrared vibrational spectroscopy to characterize the coherent vibrational dynamics of a nanoscopic ensemble of C−F vibrational oscillators of polytetrafluoroethylene (PTFE). The near-field mode transfer between the induced vibrational molecular coherence and the metallic scanning probe tip gives rise to a tip-mediated *radiative* IR emission of the vibrational free-induction decay (FID). By increasing the tip−sample coupling, we can *enhance* the vibrational dephasing of the induced coherent vibrational polarization and associated IR emission, with dephasing times up to $T_2^{NF} \simeq 370$ fs in competition against the intrinsic far-field lifetime of $T_2^{FF} \simeq 680$ fs as dominated by nonradiative damping. Near-field antenna-coupling thus provides for a new way to modify vibrational decoherence. This approach of ultrafast *s*-SNOM enables the investigation of spatiotemporal dynamics and correlations with nanometer spatial and femtosecond temporal resolution.

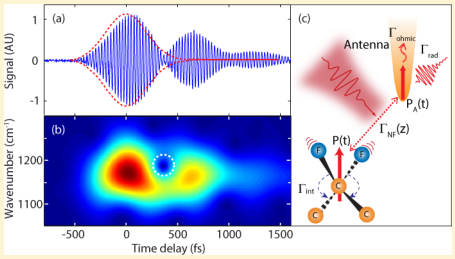

KEYWORDS: *Near-field microscopy, ultrafast infrared spectroscopy, free-induction decay, nano-optics*

Downloaded via UNIV OF COLORADO BOULDER on January 7, 2021 at 18:43:10 (UTC).
See https://pubs.acs.org/sharingguidelines for options on how to legitimately share published articles.

The aim of ultrafast spectroscopy is to characterize electron dynamics, nuclear motions, and their coupling induced by transient optical excitations in molecules and condensed matter.[1,2] The extension of ultrafast spectroscopy to two- and higher-dimensional wavemixing techniques enables the study of intra- and intermolecular coupling in the presence of structural inhomogeneities and disorder.[3,4] While the established technique of photon echo spectroscopy delivers information about the dynamics of the homogeneous subensemble, it provides no insight into the underlying spatial distribution and correlations of the inhomogeneities.[5] The combination of ultrafast spectroscopy with microscopy, however, has remained challenging[6−9] because of dispersion and aberration of the microscope optics, low signal levels, and limited k-vector control. Progress has been made to extend ultrafast microscopy beyond the optical far-field spatial resolution limit using photoelectron emission, electron diffraction, and X-ray spectroscopy.[10−12] However, the general applicability of these emergent techniques in particular to molecular and soft matter systems is still lacking, because they require special sample preparation and are instrumentally demanding.

Mid-infrared radiation couples directly to nuclear motions via IR-active vibrational modes in molecules or optical phonons in solids. In ultrafast infrared spectroscopy, structural dynamics can be probed—information otherwise not always accessible by continuous wave spectroscopies.[13] However, because of its long wavelength, the extension of IR spectroscopy into the micro- and nanoscale is particularly challenging.

In this work, we combine scattering-scanning near-field optical microscopy (*s*-SNOM) with femtosecond infrared excitation for ultrafast coherent molecular vibrational nanospectroscopy. Mid-IR femtosecond pulses have already been applied for their broad bandwidth in *s*-SNOM vibrational IR spectroscopy.[14−18] Building on these results, we demonstrate the extension of *s*-SNOM to time-domain IR vibrational nanospectroscopy. The metallic scanning probe tip localizes the infrared field to the nanoscale for a spatially confined molecular excitation. The tip in turn acquires the transient coherent vibrational polarization through near-field coupling. This leads to radiative infrared emission through the optical antenna properties of the tip. Using interferometric heterodyne amplification, we detect the associated coherent emission of the vibrational free-induction decay (FID)[19−21] of a nanoscale ensemble of molecular oscillators in a spatially confined volume of 10−20 nm radius. Increasing the near-field dipole−dipole coupling between resonant molecular excitation and the tip nano-antenna, we can increase the mode transfer between molecular and tip transient polarizations and therefore enhance the vibrational decoherence rate of the molecular excitation. The approach provides for a new way to modify vibrational coherence by antenna coupling and extends ultrafast IR spectroscopy to the nanoscale for spatiotemporal vibrational imaging on femtosecond time and nanometer length scales.

Received: December 31, 2012
Revised: January 31, 2013
Published: February 6, 2013

 © 2013 American Chemical Society dx.doi.org/10.1021/nl304804p | *Nano Lett.* 2013, 13, 1588−1595

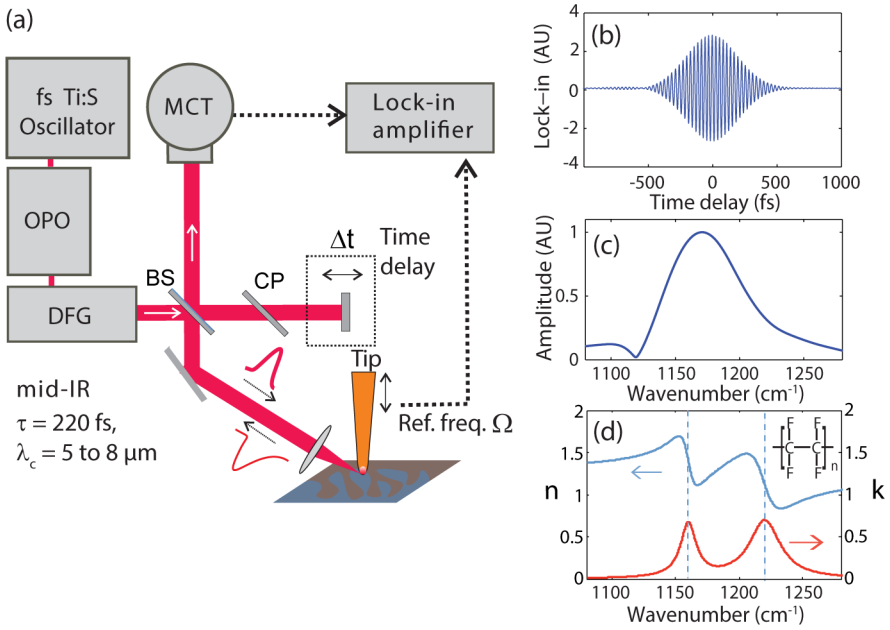

Figure 1. Femtosecond infrared vibrational scattering-scanning near-field optical microscopy (*s*-SNOM). Experimental setup (a). Interferogram of the 220 fs mid-IR laser pulse (b), with Fourier transform of the interferogram (c). Wavenumber dependence of refractive index n and absorption coefficient k of PTFE (d) are characterized by C−F symmetric and antisymmetric modes at ν_1 = 1160 cm^{-1} and ν_2 = 1220 cm^{-1}, respectively.[24]

Experiment. A schematics of our experiment is shown in Figure 1a. Mid-infrared femtosecond radiation, tunable from 5 to 10 μm, with an average power of ∼1 mW, pulse duration of ∼220 fs, and bandwidth of ∼50−100 cm^{-1} (fwhm) is obtained by difference frequency generation in GaSe,[22] of the signal and idler output of an optical parametric oscillator (OPO, Chameleon, APE, Germany) pumped by a high power femtosecond Ti:S laser (MIRA, Coherent, 3.5 W). The IR beam is collimated to a diameter of ∼10 mm, passes through a beam splitter (BS), and is focused by a parabolic mirror (focal length f = 25 mm, effective NA = 0.25, spot size diameter ∼20 μm) onto the scanning probe tip of an atomic force microscope (AFM, Innova, Bruker Inc.) modified for *s*-SNOM. The AFM is operated in dynamic noncontact mode, and platinum coated AFM probes (Arrow NCPT, Nanosensors) are used for the experiments. The tip cantilever oscillates at a frequency of $\Omega \approx$ 254 kHz with an estimated tapping amplitude of 25 nm.

The IR light is p-polarized with respect to the tip shaft. The tip-scattered light is collected in epi-detection, interferometrically heterodyned[23] with the reference field with variable time delay through a dispersion compensation plate (CP), and detected by an MCT detector (J15D12 M204 Judson). A lock-in amplifier (HF2Li, Zurich Instruments, Switzerland) is used for signal demodulation with the reference frequency set to the tip oscillation frequency Ω. Multiple harmonics ($n\Omega$, n = 1, 2, 3, ...) of the optical signal are simultaneously recorded while scanning the reference mirror position for heterodyne recording of the interferograms.

Figure 1b shows the interferometric linear autocorrelation of a typical mid-IR pulse, corresponding to a duration of ∼220 fs. Figure 1c shows the Fourier transform of that pulse with a central wavenumber of 1170 cm^{-1} and a fwhm bandwidth of 70 cm^{-1}. In our linear optical experiment, the interpretation of the ultrafast dynamics is based on the assumption that the IR laser pulse is fully spatially and temporally coherent.

We chose a flat sample of polytetrafluoroethylene (PTFE, trade name Teflon) as a model system, for the high transition dipole moment of the C−F bond and high oscillator density. Figure 1d shows the complex refractive index $\tilde{n} = n + ik$ of PTFE obtained from the literature.[24] The two dominant vibrational modes are ν_1 = 1160 cm^{-1} (symmetric stretch) and ν_2 = 1220 cm^{-1} (antisymmetric stretch).[25] For enhanced tip−sample coupling efficiency, we evaporate a gold film with a thickness gradient up to a few tens of nanometers onto the PTFE samples, forming isolated gold clusters at low coverage that percolate with increasing nominal film thickness.

Results. The measurement and analysis of the FID interferograms of time-domain *s*-SNOM directly allow for IR vibrational nanospectroscopy.[18] As an example, Figure 2a (blue trace) shows an *s*-SNOM interferogram detected at the second-harmonic (2Ω) of the cantilever oscillation with the tip engaged in noncontact mode feedback with the PTFE sample. As a reference, we use the spectrally broad-band and nonresonant near-field response from a gold surface. The envelope of its interferogram acquired under otherwise identical experimental conditions is shown in part a (dashed red). A clear resonant near-field FID behavior is discerned. The FID trace is dominated by ν_1, with a weaker signal contribution from ν_2, as seen from the Fourier transform in Figure 2b. The vibrational levels are indicated by blue dashed lines (for corresponding results with the central wavelength tuned toward ν_2, see the Supporting Information, Figure S1). The beating observed in the FID interferogram is due to the interference of these two modes with each other and with the nonresonant signal contributions.

As opposed to conventional symmetric Fourier transform infrared (FTIR) spectroscopy interferograms, the Fourier transform of the asymmetric FID interferograms directly provides the spectral amplitude and phase of the different vibrational modes.[18] The resulting normalized spectral amplitude (c) and baseline corrected spectral phase (d) exhibit dispersive vs absorptive behavior, respectively, as is characteristic for *s*-SNOM[18,26] in particular, or coherent spectroscopy in general.[27] Due to the large C−F oscillator strength and bulk

dx.doi.org/10.1021/nl304804p | *Nano Lett.* 2013, 13, 1588−1595

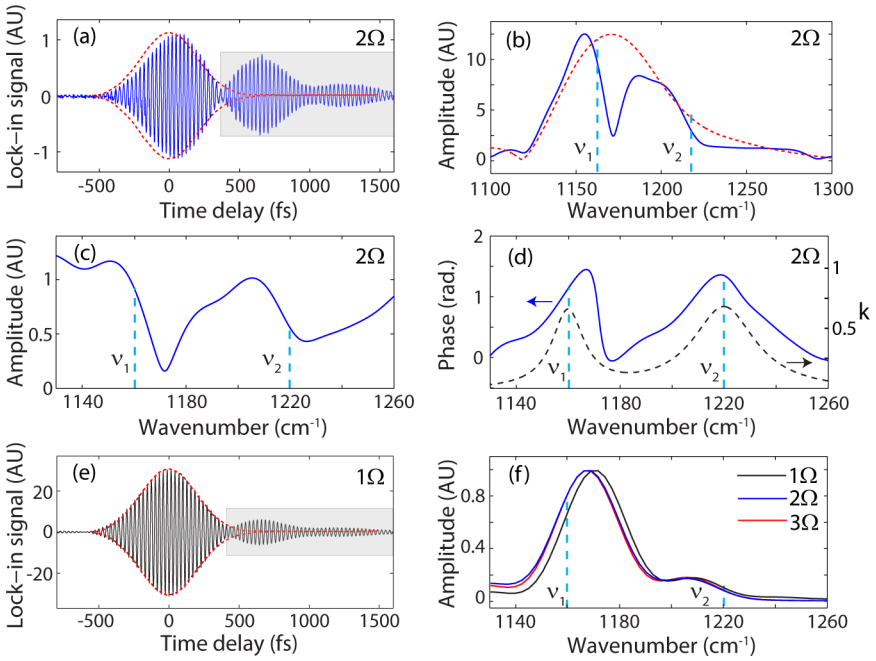

Figure 2. Vibrational near-field free-induction decay (FID) and Fourier transforms. Heterodyne near-field interferogram at 2Ω demodulation (a, blue) with nonresonant reference (envelope, red dashed). Corresponding Fourier transform with spectral amplitude of signal and laser pluse (b). Corresponding and normalized spectral amplitude (c) and baseline corrected phase (d, solid line). FTIR absorption spectrum of PTFE from the literature[24] (black dashed) with symmetric ν_1 and antisymmetric ν_2 C−F modes. Interferogram from the first harmonic demodulation at Ω (e). Fourier transform of the FID tail (f) from different harmonics shows FID is dominated by the resonant near-field signal.

sample volume, in contrast to, e.g., surface monolayer,[18] the spectral *s*-SNOM phase deviates from the absorptive line shape and peak position, in particular for the stronger ν_1 mode (FTIR absorption spectrum shown as a dashed line for comparison).

The imaginary part of the *s*-SNOM signal is approximately linearly proportional to $k(\omega)$, with $k(\omega)$ being the molecular extinction coefficient.[17,26,28] However, compared to the polar coordinate representation of amplitude and phase, in Cartesian coordinates of real and imaginary parts, the lineshapes and peak positions are more sensitive to experimental uncertainties.[29]

A significant benefit of femtosecond time-domain *s*-SNOM with pulse durations shorter than the vibrational dephasing time is that it provides for a direct way to temporally separate the resonant near-field signal from a large nonresonant near-field and far-field background. While the nonresonant response is instantaneous, the FID tail is largely dominated by the resonant near-field signal. This temporal characteristics have already been observed for the case of *s*-SNOM of long-lived phonon polariton in solids.[15]

We extend this approach to the case of a pulse duration shorter than the few hundred femtosecond molecular vibrational dephasing times. Figure 2e shows that this approach can already be applied for the first harmonics *s*-SNOM signal of PTFE. Albeit overall dominated by the instantaneous background signal, the interferogram exhibits superior signal intensity and signal-to-noise ratio of the FID tail compared to the higher harmonics.

Figure 2f shows the Fourier transform of the FID tail for delay times after the end of the exciting laser pulse. It exhibits a resonant peak corresponding to the predominantly excited ν_1 mode at the center laser wavelength. The contribution of ν_2 is further suppressed due to its faster dephasing time. The peak profile is nearly indistinct from the corresponding Fourier transforms of the higher harmonics, e.g., 2Ω (blue) and 3Ω (red) signals, where the far-field background is suppressed due to the higher-harmonic demodulation (see the Supporting Information, Figures S2 and S3, for approach curves and interferograms of different harmonics). The FID signal in first harmonic detection provides about an order of magnitude larger signal compared to the conventional higher-harmonics demodulation approach for near-field extraction. The signal spectrum in this case does not exhibit the dispersive profile characteristic of the full interferogram analysis where the dispersive spectral intensity is a result of the interference of the resonant and nonresonant near- and far-field signals. The absence of any interfering nonresonant contributions thus leads to symmetric spectral lineshapes.

The spectral shifts in the near-field phase and amplitude spectra compared to the incoherent linear absorption spectrum are due to a combination of near-field tip−sample coupling, uncertainties in *s*-SNOM interferometer calibration, and possible structural sample differences, e.g., in terms of different degrees of crystallinity of the PTFE used for the *s*-SNOM experiment compared to the samples used for the ellipsometry measurements.[24]

Following the ultrafast pump pulse excitation, coherent polarization (primarily the first order) is transferred between the excited molecules and the metallic tip as a result of the evanescent near-field tip−sample coupling. The tip behaves as a broad band nano-antenna, enhancing not only the excitation of the coherent vibrational polarization but also the mode transformation of vibrational near-field polarization into far-field radiation.[30] This coupling and vibrational energy transfer between the excited molecules and antenna modes of the tip should increase the vibrational relaxation rate and decrease the vibrational coherence time. From the FID tail of the time-resolved near-field interferogram (Figure 2a), we can directly estimate a vibrational dephasing time of T_2 = 630 ± 10 fs for

dx.doi.org/10.1021/nl304804p | *Nano Lett.* 2013, 13, 1588−1595

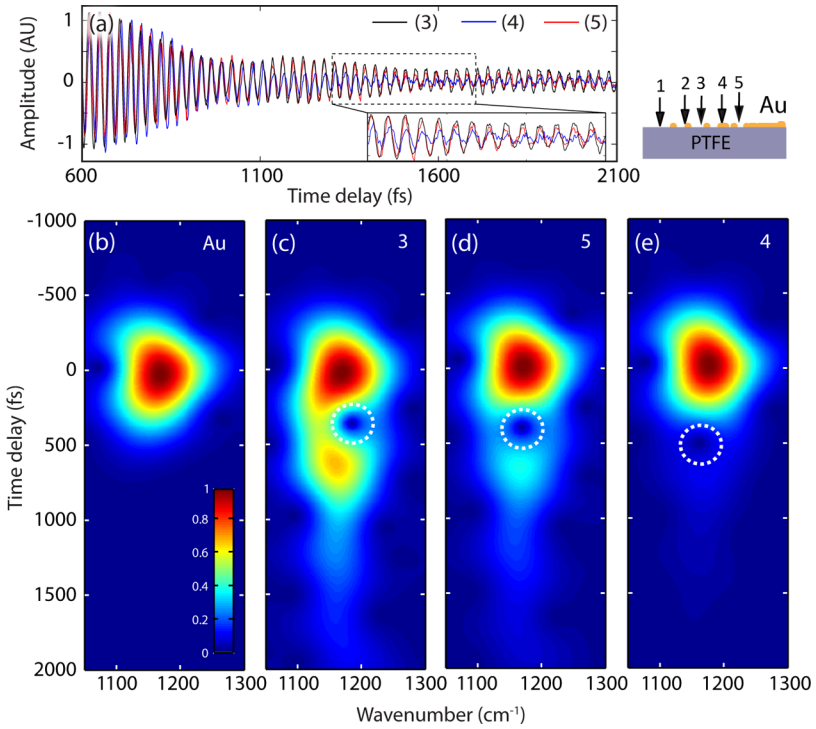

Figure 3. Effect of near-field tip−sample coupling on the radiative free-induction decay. With increasing tip−sample coupling mediated by isolated to percolated gold clusters, the dephasing time of the FID signal decreases (a) from T_2 = 610 fs (position 3) to T_2 = 540 fs (position 5) to T_2 = 370 fs (position 4). Corresponding short-time Fourier transformation of the laser spectrum (b) and PTFE FID signals (c−e). The dotted circle highlights a spatiotemporal interference feature.

ν_1.[31] This value seems reduced compared to $T_2^{FF} \simeq 680 \pm 30$ fs derived from the line width of the C−F far-field absorption spectra.

The efficiency of the polarization transfer from the vibrational excitation into both radiative and nonradiative modes of the tip can be modified by increasing the effective antenna mode volume of the tip and/or increasing the tip−sample dipole coupling efficiency. Using the PTFE sample coated with gold clusters, this gives rise to an increase in field localization and nano-antenna vibrational mode interaction. Figure 3a shows segments of the corresponding tip-scattered near-field FID behavior at different sample locations ranging from isolated (3, with similar behavior observed for positions 1 and 2, data not shown) to percolated (4, 5) gold clusters within a few micrometers of spatial separation. The interferogram intensities of the three different locations are normalized with respect to the amplitude of the second interferogram envelope maxima at 660 fs. With increasing gold particle density, an increasingly faster near-field vibrational signal decay is observed.

To better visualize the underlying spectral and temporal evolution of the vibrational FID, we perform a short-time Fourier transform[18,32,33] using a Gaussian gate function of 200 fs duration to construct a spectrogram. Figure 3c−e shows the resulting spectrograms in comparison with the corresponding laser interferogram of Figure 3b. A marked decrease in vibrational lifetime can be discerned with increasing effective gold coverage from an initially weakly perturbed $T_2 = 630 \pm 10$ fs to 610 ± 10 fs at position (3), 540 ± 10 fs at position (5), and 370 ± 10 fs at position (4). The feature marked by white circles around 400 fs is due to interference and red-shifts as the relative spectral weight of resonant to nonresonant signal contributions changes with decreasing T_2.

The different vibrational decoherence times are plotted in Figure 4a as a function of the total noninterferometric *s*-SNOM

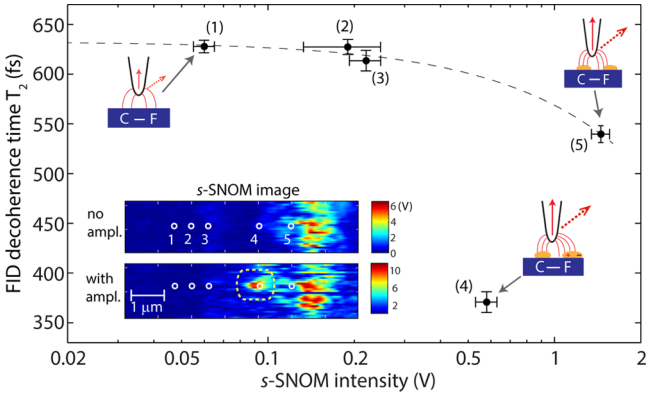

Figure 4. Enhancement of vibrational decoherence by near-field coupling. Decrease of observed decoherence time T_2 vs spectrally integrated homodyne *s*-SNOM intensity at different sample locations (dashed line as a guide to the eye). Insets: *s*-SNOM images with and without heterodyne amplification of the corresponding sample area. The unusually short dephasing at location (4) suggests an extrinsic resonant behavior of the gold nanostructure at the C−F resonance frequency. This can give rise to very strong mode transfer yet moderate intensity due to destructive signal interference.

intensities measured at the respective sample positions as indicated. A general correlation is seen between the decrease of T_2 and an increase in *s*-SNOM intensity. While the increase in total *s*-SNOM is solely due to the increase in gold particle density and corresponding field enhancement, this is equivalent to an increase in mode volume and/or near-field coupling

dx.doi.org/10.1021/nl304804p | *Nano Lett.* 2013, 13, 1588−1595

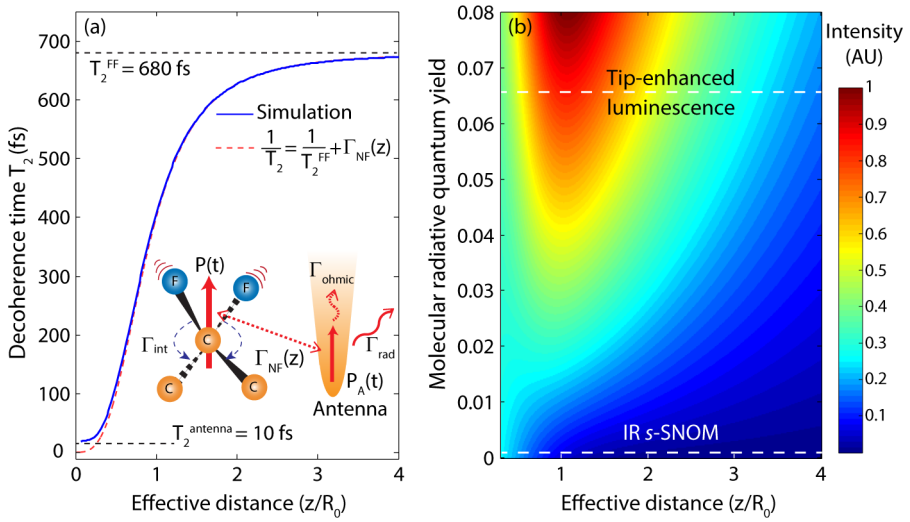

Figure 5. Decoherence time and radiative intensity vs near-field coupling. Calculated decoherence time T_2 vs effective distance z/R_0 describing the near-field mode transfer $\Gamma_{NF}(z)$ (a). Dependence of expected radiative *s*-SNOM signal as a function of coupling efficiency (b). The different regimes of emission enhancement vs quenching depend on the intrinsic molecular radiative quantum yield Φ. The behavior for typical values of tip radius r = 20 nm, critical distance R_0 = 3 nm, and antenna radiative quantum yield of 50% is given as an example (a, solid line). This corresponds to the general condition of the vibrational FID *s*-SNOM experiment (b, lower white dashed line) with low intrinsic radiative quantum yield, and with a monotonic increase in radiative intensity with increasing near-field coupling. Higher intrinsic molecular quantum yield Φ exhibits quenching at short effective distance, as in the case of tip-enhanced luminescence (b, upper white dashed line).

efficiency through which the energy is transferred, leading to a more effective decay of the molecular polarization.

Interestingly, the lowest value of T_2 = 370 fs measured at location (4) (see Figure 4) deviates from that trend with an unexpectedly low apparent total *s*-SNOM intensity. The upper inset shows a homodyne intensity *s*-SNOM scan in comparison with one using phase-sensitive interferometric heterodyne amplification (below) of the corresponding sample area with the different interferometric FID measurement locations indicated. In the latter, a larger signal at location (4) (dashed area) compared to the other locations and compared to its noninterferometric detection is observed. This suggests that the induced polarization at location (4) is out of phase with respect to the other locations due to, e.g., an extrinsic IR antenna resonance in the metallic nanostructure at that point. Such an antenna resonance would strongly increase the electromagnetic density of states in close proximity to the molecules, thus providing for an efficient dephasing channel for the molecular polarization.

Discussion. The near-field response and resulting light scattering due to the near-field tip−sample coupling can qualitatively be modeled by treating the tip as a small polarizable sphere in the quasi-static limit ($d \ll \lambda$) positioned in close proximity to the sample. The image dipole of the tip reflects the local dielectric function of the sample with its resonances.[26,34,35] In this image dipole model, the far-field excitation of the tip efficiently induces the coherent molecular polarization in the field-enhanced near-field region of the apex. This induced coupled polarization of tip apex and sample collectively and coherently emits the detectable radiation.

Assuming a broadband coherent pump pulse, we can qualitatively describe the profile of the observed FID behavior in either the frequency or the time domain (see the Supporting Information, Figure S5). The near-field signal is a coherent superposition of a frequency independent nonresonant instantaneous response and the resonant vibrational contributions that maintain its coherent polarization according to its dephasing time. The image dipole model explains the spectral phase behavior observed and the characteristic dispersive amplitude profiles as a result of the interference between these different terms with corresponding real and imaginary contributions of the resonant tip−sample polarizability. In the time domain, the two vibrational resonances manifest themselves in the beating of the FID profiles (Figure 2a). Furthermore, the model reproduces the observed spectro-temporal interference feature indicated in Figure 3c (see the Supporting Information, Figure S7).

The key aspect the image dipole model does not capture is the coherent energy transfer between the molecular vibrational excitation and the antenna mode of the tip. The dynamic behavior resulting from the image dipole model is limited to the intrinsic dynamics of the sample resonances, which is assumed to be unperturbed by the local dielectric surrounding created by the presence of the metallic tip in this case.

The intrinsic radiative lifetime of a vibrational excitation can generally be ∼10 μs or more due to the large mode mismatch between molecular oscillators and the IR far-field electromagnetic density of states.[36] With typical decay times of polyatomic molecules or in condensed phase being dominated by fast nonradiative intra- and intermolecular coherent and incoherent energy transfer on picosecond time scales, radiative emission is generally very weak.[37] However, for molecules in close proximity to a metal nanostructure, near-field polarization transfer can occur via dipole−dipole coupling. This opens additional radiative and nonradiative decay channels for the vibrational excitation via the antenna modes of the tip, associated with a net decrease in vibrational lifetime.

Figure 5a (inset) shows a schematic indicating the competition between the nonradiative intramolecular decay rate Γ_{int} and the energy transfer to the antenna described by $\Gamma_{NF}(z)$. The polarization transfer between the coherent molecular excitation $P(t)$ and the antenna polarization $P_A(t)$ can be described through a set of coupled rate equations given by

dx.doi.org/10.1021/nl304804p | Nano Lett. 2013, 13, 1588−1595

$$\frac{dP(t)}{dt} = -[\Gamma_{int} + \Gamma_{mrad} + \Gamma_{NF}(z)]P(t) + \Gamma_{NF}(z)P_A(t) \quad (1)$$

with Γ_{mrad} being the molecular radiative decay rate, and

$$\frac{dP_A(t)}{dt} = -[\Gamma_{ohmic} + \Gamma_{rad} + \Gamma_{NF}(z)]P_A(t) + \Gamma_{NF}(z)P(t) \quad (2)$$

with Γ_{rad} and Γ_{ohmic} describing the radiative and nonradiative damping of the antenna, respectively.

Without loss in generality, we describe the near-field coupling and mode transfer $\Gamma_{NF}(z)$ between the molecular excitation and the metallic tip by dipole−dipole coupling with an effective distance dependence, similar to molecular energy transfer in fluorescence resonant energy transfer (FRET) as $\Gamma_{NF}(z) \propto (1/\tau_{nf})(R_0/z)^n$. The distance z and critical distance R_0 are on the order of the tip apex radius consistent with the near-field tip−sample distance dependence, and the exponent n is between 3 and 6 depending on the size and dimensionality of the coupled elements. The metal nanostructure, with polarizability proportional to its mesoscopic volume, and possibly enhanced via resonant plasmon or antenna modes, exhibits a greatly improved coupling to the far-field density of states.[38] In contrast to the visible spectral range, at IR frequencies, Pt has a high optical conductivity comparable to Au and Ag. Following Mie theory, effective radiative (optical antenna effect) emission is expected, possibly exceeding the nonradiative (ohmic) loss with $1/\Gamma_{ohmic} \approx 20$ fs given by the Drude relaxation time (refs 36 and 39 and references therein).

Assuming $1/(\Gamma_{ohmic} + \Gamma_{rad}) = T_2^{antenna} \simeq 10$ fs (i.e., antenna radiative quantum yield of $\Phi = 50\%$), $\Gamma_{mrad} \approx 0$ fs^{-1}, and $n = 3$, from solving the coupled rate equations, we can derive the change in molecular dephasing time T_2 with increasing near-field antenna coupling, as shown in Figure 5a. For large tip−sample separation and hence weak evanescent near-field coupling to the tip, T_2 asymptotically approaches the primarily nonradiative far-field C−F vibrational relaxation time $T_2^{FF} = 1/\Gamma_{int} \approx 680$ fs (top horizontal dotted line). In the limit of strong coupling and efficient mode transfer to the tip, the molecular damping becomes rate limited only by the antenna damping and the dephasing time approaches that of the antenna $T_2^{antenna} \simeq 10$ fs. With almost 2 orders of magnitude faster antenna damping compared to the molecular damping, under the weak near-field coupling condition, the behavior can be approximated by $1/T_2 = 1/T_2^{FF} + \Gamma_{NF}(z)$ (dashed red curve).

Due to the fast antenna relaxation compared to molecular dephasing, we can assume a steady state condition $dP_A(t)/dt \approx 0$ for a wide range of coupling efficiencies $\Gamma_{NF}(z)$. From eq 2, we then obtain

$$\frac{P_A(t)}{P(t)} = \frac{\Gamma_{NF}(z)}{\Gamma_{ohmic} + \Gamma_{rad} + \Gamma_{NF}} \quad (3)$$

which reflects the partition of the induced coherent polarization between molecular vibrations and tip/antenna electronic polarization. With the radiative emission $S_{NF}(t) \propto \Gamma_{rad}P_A(t) + \Gamma_{mrad}P(t)$, we then obtain a steady state solution for the radiative *s*-SNOM signal given by

$$S_{NF}(t) \propto \left[\frac{\Gamma_{rad}\Gamma_{NF}(z)}{\Gamma_{ohmic} + \Gamma_{rad} + \Gamma_{NF}(z)} + \Gamma_{mrad}\right]P(t) \quad (4)$$

for the general case including finite values for Γ_{mrad}.

From eq 4, we can see that the near-field signal in the time domain $S_{NF}(t)$ is directly proportional to the molecular polarization $P(t)$. In addition to the acceleration of the molecular vibrational decoherence, $\Gamma_{NF}(z)$ is responsible for the conversion of the molecular evanescent near-field molecular polarization into detectable far-field emission. Surface metallization has the equivalent function of decreasing the tip−sample distance, improving the mode overlap and/or mode volume of the antenna via the effective $\Gamma_{NF}(z)$.

Such metal-enhanced vibrational molecular decoherence and radiative emission is on a fundamental level analogous to the competition between field enhancement and quenching of the fluorescence of molecules or atoms coupled to a metal surface[40] or plasmonic nanostructure.[41] For its unified description, we consider that, concurrent with the decrease in decoherence time, the local field enhancement $\mathcal{F}$ at the tip gives rise to an increase in excitation rate. Here, the tip dipole acquires the far-field excitation E_{inc} and drives the molecules in the sample coherently with increased efficiency depending on the local field strength $E_{loc} \propto \mathcal{F}E_{inc}$. However, despite the tip-induced increase in excitation rate and decrease in molecular lifetime, the overall radiated signal intensity increase is limited by unavoidable ohmic damping which is a significant fraction of the transferred polarization to the tip.

In contrast to the inefficient far-field infrared vibrational emission, molecular electronic fluorescence exhibits appreciable free-space radiative emission on nanosecond time scales (high quantum yield), with comparably weak nonradiative intramolecular decay pathways expressed through the molecular radiative quantum yield $\Phi = \Gamma_{mrad}/(\Gamma_{int} + \Gamma_{mrad})$. Introducing an empirical tip−sample distance dependence for the local field enhancement $\mathcal{F} \propto 1/(r + z)^3$ with tip radius r, we can extend the model calculation from above to derive the expected radiative *s*-SNOM intensity as a function of quantum yield and tip−sample distance, as shown in Figure 5b.

For appreciable quantum yields, molecular fluorescence undergoes a crossover from an intensity increase due to field enhancement and a higher excitation rate to an intensity decrease at close proximity between the molecule and the metal dominated by its nonradiative damping. In contrast to electronic fluorescence, for vibrational excitation with negligible intrinsic molecular radiative damping, any degree of coupling via $\Gamma_{NF}(z)$ will open the radiative decay channel Γ_{rad} as the only radiative emission pathway. Hence, with increasing coupling Γ_{NF} to the tip/nanostructure, the radiative emission will increase monotonically, associated with a decrease in molecular dephasing time T_2 (lower white dashed line).

This ability to effectively transfer evanescent near-field polarization into far-field radiation by antenna coupling has interesting implications on coherent spectroscopy. In conventional coherent wave-mixing experiments, the induced coherent vibrational polarization is probed by successive laser pulses to generate a photon echo[42] or by frequency up-conversion as in the case of sum-frequency generation.[43] In the near-field approach, the antenna coupling directly generates the detectable far-field signal which is proportional to $P(t)$, with $S_{NF}(t) \propto P(t)$; i.e., the scattered resonant near-field signal has the same temporal behavior as the molecular polarization. Therefore, combining the nanospectroscopic *s*-SNOM capability with appropriate ultrafast wave-mixing techniques, femtosecond coherent spectroscopy can be extended to the nanoscale, providing enhanced sensitivity and nanometer

dx.doi.org/10.1021/nl304804p | Nano Lett. 2013, 13, 1588−1595

spatial resolution. This includes multidimensional spectroscopy, in, e.g., photon echo implementation, potentially giving insight into the spatiotemporal dynamics and coupling on the nanometer–femtosecond scale.

s-SNOM can be further improved in sensitivity by designing antennas for near-field nanospectroscopy with increased Γ_{rad}. The extension to the use of resonant plasmonic or antenna modes in the tips would provide higher field enhancement and greatly improve the coupling to the far-field density of states; however, the temporal convolution, phase effects and interference, and resonant splitting might complicate signal interpretation.[44] A similar effect of reduced vibrational coherence time would be expected in surface-enhanced infrared absorption (SEIRA), yet even for the case of vibrational overlap with resonant IR antenna modes of the metal nanostructure, the signal is still dominated by a spatial average over an extended near-field region, making the observation difficult.[45,46]

Conclusion. Our results of tip-induced radiative infrared vibrational molecular emission with enhancement of the radiative free-induction decay rate by tip–sample coupling is to the best of our knowledge the first such observation in vibrational spectroscopy. Taking advantage of the optical antenna properties and field localization of metallic scanning probe tips improves mode matching between the near-field molecular oscillator polarization and far-field density of states. This results in enhanced sensitivity of coherent IR spectroscopy compared to conventional far-field spectroscopy. The process can be further tuned by controlling the coupling efficiency between molecular dipole and antenna, and the design of selective IR plasmonic antenna resonances in the tip at the molecular resonance frequency. This provides a new handle to modify molecular vibrational decoherence by the antenna-induced near-field coupling. Under weak near-field coupling, the radiative emission of the tip can produce an echo equivalent signal as desired for two-dimensional infrared spectroscopy. By suitable tailoring of infrared laser excitation pulses,[47] and with heterodyne detection on the resonant near-field scattering with a reference pulse, it is in principle possible to implement coherent two-dimensional infrared spectroscopy in the nanoscale with *s*-SNOM. This would open the possibility of elucidating underlying mechanisms of homogeneous and inhomogeneous broadening in heterogeneous media. Under the strong near-field coupling regime, the coherent implementation of nanoparticle-enhanced 2D infrared spectroscopy is expected to provide interesting complementary results to our work.[48]

■ ASSOCIATED CONTENT

Ⓢ Supporting Information

Additional information and figures related to vibrational near-field response, near-field vertical and lateral spatial localization, interferogram envelope progression with lock-in demodulation harmonics, and model calculation. This material is available free of charge via the Internet at http://pubs.acs.org.

■ AUTHOR INFORMATION

Corresponding Author

*E-mail: markus.raschke@colorado.edu.

Notes

The authors declare no competing financial interest.

■ ACKNOWLEDGMENTS

We would like to thank Andrew Jones, Rob Olmon, Brian O'Callan, Ben Pollard, and Ian Craig for valuable discussions and support at various stages of the experiments. Honghua Yang has provided invaluable theoretical support. Funding was provided by the National Science Foundation (NSF CAREER Grant CHE 0748226) and a partner proposal by the Environmental Molecular Sciences Laboratory (EMSL), a national scientific user facility from DOE's Office of Biological and Environmental Research at Pacific Northwest National Laboratory (PNNL). PNNL is operated by Battelle for the US DOE under the contract DEAC06-76RL01830.

■ REFERENCES

(1) Zewail, A. H. *Femtochemistry: Ultrafast Dynamics of the Chemical Bond*; World Scientific: Singapore, 1994.
(2) Engel, G. S.; Calhoun, T. R.; Read, E. L.; Ahn, T. K.; Mancal, T.; Cheng, Y. C.; Blankenship, R. E.; Fleming, G. R. *Nature* **2007**, *446*, 782–786.
(3) Hamm, P.; Lim, M. H.; Hochstrasser, R. M. *J. Phys. Chem. B* **1998**, *102*, 6123–6138.
(4) Zanni, M. T.; Hochstrasser, R. M. *Curr. Opin. Struct. Biol.* **2001**, *11*, 516–522.
(5) Cho, M. H. *Chem. Rev.* **2008**, *108*, 1331–1418.
(6) Mehl, B. P.; Kirschbrown, J. R.; House, R. L.; Papanikolas, J. M. *J. Phys. Chem. Lett.* **2011**, *2*, 1777.
(7) Terada, Y.; Yoshida, S.; Takeuchi, O.; Shigekawa, H. *Nat. Photonics* **2010**, *4*, 869–874.
(8) Raghunathan, V.; Han, Y.; Korth, O.; Ge, N. H.; Potma, E. O. *Opt. Lett.* **2011**, *36*, 3891–3893.
(9) Frontiera, R. R.; Henry, A. I.; Gruenke, N. L.; Van Duyne, R. P. *J. Phys. Chem. Lett.* **2011**, *2*, 1199–1203.
(10) Zewail, A. H. *Annu. Rev. Phys. Chem.* **2006**, *57*, 65.
(11) Kubo, A.; Pontius, N.; Petek, H. *Nano Lett.* **2007**, *7*, 470–475.
(12) Aeschlimann, M.; Brixner, T.; Fischer, A.; Kramer, C.; Melchior, P.; Pfeiffer, W.; Schneider, C.; Strüber, C.; Tuchscherer, P.; Voronine, D. V. *Science* **2011**, *333*, 1723–1726.
(13) Khalil, M.; Demirdoven, N.; Tokmakoff, A. *J. Phys. Chem. A* **2003**, *107*, 5258–5279.
(14) Brehm, M.; Schliesser, A.; Keilmann, F. *Opt. Express* **2006**, *14*, 11222–11233.
(15) Amarie, S.; Ganz, T.; Keilmann, F. *Opt. Express* **2009**, *17*, 21794–21801.
(16) Amarie, S.; Keilmann, F. *Phys. Rev. B* **2011**, *83*, 045404.
(17) Huth, F.; Govyadinov, A.; Amarie, S.; Nuansing, W.; Keilmann, F.; Hilenbrand, R. *Nano Lett.* **2012**, *12*, 3973–3978.
(18) Xu, X. G.; Rang, M.; Craig, I. M.; Raschke, M. B. *J. Phys. Chem. Lett.* **2012**, *3*, 1836–1841.
(19) Crowell, R. A.; Holtom, G. R.; Xie, X. S. *J. Phys. Chem.* **1995**, *99*, 1840–1842.
(20) Rhee, H.; June, Y. G.; Kim, Z. H.; Jeon, S. J.; Cho, M. *J. Opt. Soc. Am. B* **2009**, *26*, 1008–1017.
(21) Rhee, H.; Choi, J. H.; Cho, M. *Acc. Chem. Res.* **2010**, *43*, 1527–1536.
(22) Ehret, S.; Schneider, H. *Appl. Phys. B: Lasers Opt.* **1998**, *66*, 27–30.
(23) As a result of the molecular sample resonances, the broadband spectrum of the tip-scattered radiation differs from the driving laser field; hence, we prefer the term heterodyne in this work over homodyne.
(24) Korte, E. H.; Roseler, A. *Anal. Bioanal. Chem.* **2005**, *382*, 1987–1992.
(25) Starkweather, H. W.; Ferguson, R. C.; Chase, D. B.; Minor, J. M. *Macromolecules* **1985**, *18*, 1684–1686.
(26) Knoll, B.; Keilmann, F. *Opt. Commun.* **2000**, *182*, 321–328.
(27) Xu, X. J. G.; Konorov, S. O.; Hepburn, J. W.; Milner, V. *Opt. Lett.* **2008**, *33*, 1177–1179.

(28) Mueller, K.; Yang, X. J.; Paulite, M.; Fakhraai, Z.; Gunari, N.; Walker, G. C. *Langmuir* **2008**, *24*, 6946−6951.
(29) In phase and amplitude coordinates, a phase change does not affect the amplitude and leads to only a general phase offset of the spectrum. In Cartesian complex coordinates, the Im and Re of the signal are coupled, with a phase uncertainty sensitively affecting the spectral line shape. Furthermore, due to the finite bandwidth of the laser pulse (∼70 cm^{-1}) compared to the spectral linewidths of the vibrational resonances, baseline correction of the phase is difficult, requiring clear spectral distinction of the nonresonant near-field signal.
(30) Alonso-Gonzalez, P.; Albella, P.; Schnell, M.; Chen, J.; Huth, F.; Garcia-Etxarri, A.; Casanova, F.; Golmar, F.; Arzubiaga, L.; Hueso, L. E.; Aizpurua, J.; Hillenbrand, R. *Nat. Commun.* **2012**, *3*, 684.
(31) The dephasing time is determined from an exponential fit of the interferogram after the second maxima, i.e., where the nonresonant near-field, residual far-field, and ν_2 contributions are temporally separated from the resonant near-field response from ν_1. Note that due to the presence of the, albeit weakly excited and faster decaying ν_2 level, the value of T_2 for ν_1 could be slightly underestimated.
(32) Rioul, O.; Flandrin, P. *IEEE Trans. Signal Process.* **1992**, *40*, 1746−1757.
(33) Lang, W. C.; Forinash, K. *Am. J. Phys.* **1998**, *66*, 794−797.
(34) Raschke, M. B.; Lienau, C. *Appl. Phys. Lett.* **2003**, *83*, 5089−5091.
(35) Keilmann, F.; Hillenbrand, R. *Philos. Trans. R. Soc. London, Ser. A* **2004**, *362*, 787−805.
(36) Olmon, R. L.; Raschke, M. B. *Nanotechnology* **2012**, *23*, 444001.
(37) Nesbitt, D. J.; Leone, S. R. *Chem. Phys. Lett.* **1982**, *87*, 123−127.
(38) Berweger, S.; Atkin, J. M.; Raschke, M. B. *J. Phys. Chem. Lett.* **2012**, *3*, 945.
(39) Jones, A. C.; Olmon, R. L.; Skrabalak, S. E.; Wiley, B. J.; Xia, Y. N.; Raschke, M. B. *Nano Lett.* **2009**, *9*, 2553.
(40) Drexhage, K. H. *Prog. Opt* **1974**, *12*, 163.
(41) Anger, P.; Bharadwaj, P.; Novotny, L. *Phys. Rev. Lett.* **2006**, *96*, 113002.
(42) Jonas, D. M. *Annu. Rev. Phys. Chem.* **2003**, *54*, 425−463.
(43) Shen, Y. R. *Nature* **1989**, *337*, 519−525.
(44) Chen, K.; Adato, R.; Altug, H. *ACS Nano* **2012**, *6*, 7998−8006.
(45) Kundu, J.; Le, F.; Nordlander, P.; Halas, N. J. *Chem. Phys. Lett.* **2008**, *452*, 115−119.
(46) Neubrech, F.; Pucci, A.; Cornelius, T. W.; Karim, S.; Garcia-Etxarri, A.; Aizpurua, J. *Phys. Rev. Lett.* **2008**, *101*, 157403.
(47) Shim, S. H.; Strasfeld, D. B.; Zanni, M. T. *Opt. Express* **2006**, *14*, 13120−13130.
(48) Donaldson, P. M.; Hamm, P. *Angew. Chem., Int. Ed.* **2012**, *52*, 634.